Journal of Rock Mechanics and Geotechnical Engineering

Journal online: www.rockgeotech.org

Seismic response of an earth dam: finite element coupling analysis and validation from centrifuge tests

Chunhsien Wu[1], Chihkuan Ni[2*], Honyim Ko[3]

[1] *Institute of Earth Sciences, Academia Sinica, Taipei, 11529, China*

[2] *Department of Civil Engineering, Taipei University of Technology, Taipei, 10608, China*

[3] *Department of Civil, Environmental, and Architectural Engineering, University of Colorado, Boulder 80309, USA*

Received 11 December 2008; received in revised form 19 March 2009; accepted 26 April 2009

Abstract: Variations in acceleration and excess pore water pressure during a seismic event are critical early-warning indicators of an impending dam collapse. To assess these variations, the seismic responses for three simplified model dams, based on cross-sections through a real earthen dam, were assessed with numerical simulations and centrifuge tests. A normalized root-mean-square error was utilized as a comparison index to assess the closeness between simulated and the recorded values. Assuming that the experimental records are reliable, the reliability of the numerical program was evaluated using this root-mean-square error estimation approach. Explanations for inconsistency between the two approaches are presented. The conclusions are drawn from the results of the three model dams.

Key words: earth dams; centrifugal tests; earthquake; numerical simulation

1 Introduction

The physical response of earthen dams to seismic events can be used to assess their stability during earthquake-induced ground shaking. Variations of displacements, accelerations and excess pore water pressures during a seismic event can be used to provide early indication warning of an impending dam collapse. Based on one-dimensional shear slice theory [1, 2], an approximate method to evaluate the maximum horizontal crest acceleration and deformation of a slope was first proposed by Makdisi and Seed [3]. This method is based on the following assumptions: (1) deformation is due only to uniform shear stress on each horizontal strip; (2) the soil is elastic; and (3) seepage is ignored. Newmark [4] proposed a pseudo-static method to calculate the permanent slope displacements induced by actual earthquakes. In this method, a probable landslide was modeled as a block increasingly displaced along an inclined plane. The maximum ground acceleration was found to be greater than the yield acceleration of the slope. The yield acceleration could be calculated by the force equilibrium of the sliding block. Based on the Newmark-type model, more semi-empirical relationships for estimating permanent displacements of slopes due to earthquakes were proposed [5, 6]. A shortcoming with this approach, as reviewed by Ozkan [7], is that the softening effect of pore pressure accumulation, e.g. liquefaction, was not considered. In recent decades, numerical simulations using a finite element method (FEM) have been adopted to investigate the seismic behaviors of dams [8, 9]. FEM simulations handle complex boundary conditions more suitably and with more flexibility than the Newmark-type models. Excess pore water pressures and permanent deformations of a dam under seismic loading can be simulated with appropriate constitutive relationships for the nonlinear behaviors of soils in such numerical models. However, the reliability of the simulated results still needs to be evaluated.

Laboratory tests, such as the centrifugal modeling tests (CMTs) used for geotechnical problems, can provide the basis for numerical model validation. The VELACS program (verification of liquefaction analysis by centrifuge studies), funded by the U.S. National Science Foundation from 1989 to 1992, is well known for the verification of liquefaction analyses [10–12]. In this program, nine specially configured CMTs can be constructed and individually tested. The results of the CMTs are then compared with numerical modeling

Doi: 10.3724/SP.J.1235.2009.00056

*Corresponding author. Tel: +86-2-27712171-2624;

E-mail: ckni@ntut.edu.tw.

Sponsored by the Taiwan Water Corporation under the Seismic Evaluation of JenYiTan Dam project, Academia Sinica (Taipei) and the National Sciences Council under Grant (NSC94-2119-M-001-016)

results [13, 14].

To better understand the seismic response of dams with varying water levels (e.g. from upstream and downstream locations) and the methods required to collect data for validating numerical models, two teams, from University of Colorado at Boulder (UCB) and Taipei University of Technology (TUT), combined to execute three dam-style CMTs, together with the development of complementary numerical models. Modeling results obtained by using code LIQCA are described in this paper, whereas modeling results obtained by using codes DIANA-SWANDYNE2 and FLAC are presented in Refs.[15] and [16]. Using a normalized root-mean-square error (in terms of excess pore water pressure and acceleration time histories) approach, a comparative assessment of the reliability of the numerical modeling results is addressed in Section 5, with discussions on cause-and-effect relationships. Before describing the validating process, the algorithm and constitutive law in the LIQCA model are briefly explained in Section 2.

2 Coupled algorithm and constitutive law in LIQCA

The code LIQCA is based on a coupled algorithm that can simultaneously solve the accelerations ($\ddot{\boldsymbol{u}}$) of soil skeletons and the excess pore water pressure (p). According to Biot's phenomenological poroelasticity theory [17], saturated soil is modeled as a two-phase medium composed of solid and fluid phases. The governing equations are derived using the following assumptions: a small relative acceleration between soil particles and pore fluids, infinitesimal strain, smooth distribution of porosity in the soil, and incompressible soil particles and pore fluids. The equilibrium equation of the soil particles is given as

$$\rho\ddot{u}_i^{\mathrm{s}} = \sigma_{ij} + \rho b_i$$
(i = 1, 2 3; j = 1, 2 3) (1)

where ρ is the density of the saturated medium, σ_{ij} is the stress tensor, b_i is the body force, and $\ddot{u}_i^{\mathrm{s}}$ is the displacement vector of the solid phase.

The continuity equation of the pore fluid is given as

$$\rho^{\mathrm{f}}\ddot{u}_{i,i}^{\mathrm{s}} = p_{ii} + \frac{\gamma_{\mathrm{w}}}{k}\dot{\varepsilon}_{ii} \tag{2}$$

where $\dot{\varepsilon}_{ii}$ is the strain tensor, k is the permeability, and γ_{w} is the unit weight of water. The superscripts "s" and "f" denote the soil skeleton and pore fluids, respectively. In the tensor notation, partial derivatives are denoted by a comma. Superscript dots denote the degree of the differential for time.

Using the Galerkin discretization method, Eqs.(1) and (2) are spatially discretized and combined into a matrix form as

$$\begin{bmatrix} \boldsymbol{M}_{uu} & 0 \\ \boldsymbol{M}_{up} & 0 \end{bmatrix}\begin{Bmatrix} \ddot{\boldsymbol{u}}_N \\ \ddot{p}_N \end{Bmatrix} + \begin{bmatrix} \boldsymbol{C}_{uu} & 0 \\ \boldsymbol{C}_{up} & 0 \end{bmatrix}\begin{Bmatrix} \dot{\boldsymbol{u}}_N \\ \dot{p}_N \end{Bmatrix} + \begin{bmatrix} \boldsymbol{K}_{uu} & \boldsymbol{K}_{pu} \\ 0 & \boldsymbol{K}_{pp} \end{bmatrix}\begin{Bmatrix} u_N \\ p_N \end{Bmatrix} = \begin{Bmatrix} \boldsymbol{F}_u \\ \boldsymbol{F}_p \end{Bmatrix} \tag{3}$$

where $\boldsymbol{M}$, $\boldsymbol{C}$, and $\boldsymbol{K}$ are the massive, viscous, and stiffness matrices, respectively; $\boldsymbol{F}$ is the external force vector, $\dot{\boldsymbol{u}}$ is the velocity, and $\boldsymbol{u}$ is the displacement. The subscripts "N", "u", and "p" denote the node of the element, the displacement of the soil skeleton, and the excess pore water pressure, respectively. Newmark's beta method [18] was used for temporal discretization as described by the following expression:

$$\begin{bmatrix} \boldsymbol{M}' + \beta(\Delta t)^2\boldsymbol{K}_{|t+\Delta t} & \boldsymbol{K}_{\mathrm{V}} \\ \boldsymbol{K}_V^T & -\sum\alpha_i \end{bmatrix}\begin{Bmatrix} \ddot{\boldsymbol{u}}_{N|t+\Delta t} \\ p_{|t+\Delta t} \end{Bmatrix} + \begin{Bmatrix} 0 \\ \sum\alpha_i\, p_{i|t+\Delta t} \end{Bmatrix} = \begin{Bmatrix} \boldsymbol{F}^{(1)} \\ \boldsymbol{F}^{(2)} \end{Bmatrix} \tag{4}$$

where $\boldsymbol{M}'$ is the mass matrix, $\boldsymbol{K}_{\mathrm{V}}$ is the stiffness vector against volumetric change, $\boldsymbol{F}^{(1)}$ and $\boldsymbol{F}^{(2)}$ are vectors of external force, β is a parameter of Newmark's beta method, Δt is the time step, a parameter of elemental permeable path, α_i is defined as

$$\alpha_i = -\frac{k}{r_{\mathrm{w}}}\left(\frac{2g}{2k - g\Delta t}\right)\left(\frac{by_i}{lx_i} + \frac{bx_i}{ly_i}\right) \tag{5}$$

where g is the acceleration of gravity; by_i, bx_i, ly_i, and lx_i are given in Fig.1.

The external force terms of Eq.(4) are expressed as

$$\boldsymbol{F}^{(1)} = \boldsymbol{F}_{|t+\Delta t} - \sum_{i=0}^{t}\boldsymbol{K}_i\Delta\boldsymbol{u}_{Ni} - \boldsymbol{K}_{|t+\Delta t}\left[\Delta t\dot{\boldsymbol{u}}_{N|t} + \left(\frac{1}{2} - \beta\right)\Delta t^2\ddot{\boldsymbol{u}}_{N|t}\right] \tag{6}$$

$$\boldsymbol{F}^{(2)} = \left(\frac{2g}{2k - g\Delta t}\right)\boldsymbol{K}_{\mathrm{V}}^{\mathrm{T}}\left(\dot{\boldsymbol{u}}_{N|t} + \frac{1}{2}\Delta t\ddot{\boldsymbol{u}}_{N|t}\right) \tag{7}$$

The code LIQCA is developed based on the above governing equations. Oka et al. [19] verified the accuracy of the code by comparing the numerical results to analytical solutions for the transient response of saturated porous solids.

Since soil behaves in a nonlinear, stress-path dependent, and stress-induced anisotropic manner, an elastic constitutive law is not suitable. However, based on a non-associated flow rule and nonlinear mixed hardening rules, a cyclic elastoplastic soil constitutive law was derived [20] and implemented in the LIQCA. Three main functions of the so-called Oka constitutive law are briefly described below.

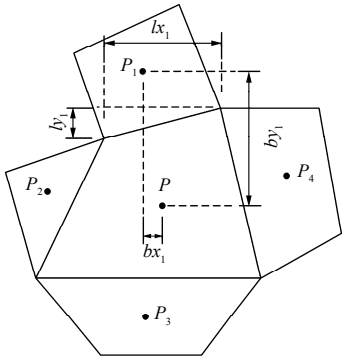

Fig.1 Schematic illustration of by_i, bx_i, ly_i, and lx_i between the considered element P and the neighboring element P_i. The lengths of edges defining element P projected horizontally and vertically are lx_i and ly_i, respectively. The horizontal and vertical distances between the gravity centers of these two connected elements are bx_i and by_i, respectively.

First, the function of the normal-consolidation boundary surface f_b is given as

$$f_b = |\eta_{ij}| + M_m \ln(\sigma'_m / \sigma'_{me}) = 0 \quad (8)$$

where η_{ij} is the stress ratio ($\eta_{ij} = s_{ij} / \sigma'_m$, s_{ij} is the deviatoric stress), σ'_m is the effective mean stress, σ'_{me} is the effective mean stress after an isotropic consolidation, and M_m is the slope of the phase transformation line or the turning-point stress ratio. σ'_{me} increases with the compressive plastic volumetric strain ε_v^p, and decreases with extended ε_v^p.

Second, the function of plastic potential surface f_p is given as

$$f_p = |\eta_{ij} - X_{ij}| + M_s \ln(\sigma'_m / \sigma'_{me}) = 0 \quad (9)$$

where M_s is the slope of the non-volumetric-strain line, X_{ij} is a variable, and X_{ij} increment changes nonlinearly with an increment of plastic deviatoric strain, i.e. de_{ij}^p, as the following expression:

$$dX_{ij} = B(M_f de_{ij}^p - X_{ij} |de_{ij}^p|) \quad (10)$$

where B is a material parameter, and M_f is the slope of critical state line or the ultimate stress ratio. In addition, $M_f > M_m \geq M_s$.

Finally, the function of the yielding surface f is

$$f = |\eta_{ij} - X_{ij}| - k_s = 0 \quad (11)$$

where k_s is the slope of yielding surface.

The lines of M_f, M_m, and M_s, and surfaces of f_b and f_p are shown in Fig.2. The two invariants of stress $I = \sigma'_{kk}/3 = \sigma'_m$ and $J = \sqrt{s_{ij}s_{ij}/2}$ are the horizontal and vertical coordinates, respectively. The initial stress gap, p_z, is defined later. To date, this constitutive law has been partially used to evaluate the behaviors of various soils [21, 22]. The constitutive law and the coupled analysis method were validated for vertical array records during the 1995 Kobe earthquake and results of shaking table tests [23, 24].

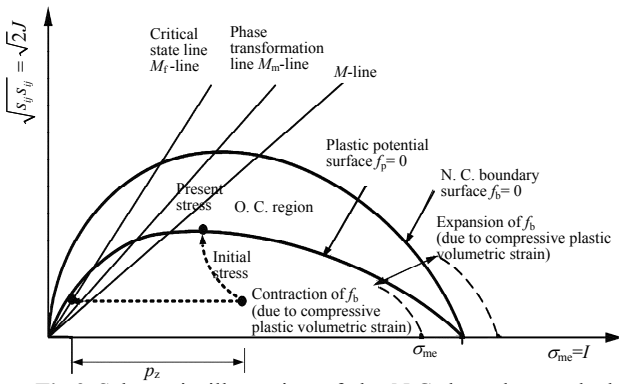

Fig.2 Schematic illustration of the N.C. boundary and plastic potential surfaces for the Oka constitutive law.

3 Centrifugal Modeling Tests

Unlike metals, the stiffness of soil is strongly affected by the confining stress. For the CMTs, the artificial centrifugal acceleration was selected as N times that of gravity (g), i.e. Ng, to raise the gravity-induced stresses in the 1/N scale models. Hereafter, N is denoted as the scaling factor of the model. Hence, the confining stress and stress-strain relationships at homologous points are identical in both reduced-scale models in the CMTs and the prototypes if the same soil is employed. Thus, the behaviors of the models should mimic the behaviors of the prototypes.

Following the centrifugal scaling laws [25], the dimension of each physical quantity can be transferred between the reduced-scale models in the CMTs and the equivalent full-scale prototypes. Therefore, reduced-scale geomechanical tests can be performed to provide data that can verify the accuracy of analytical methods for full-scale problems. However, to date, there has been no firm evidence to verify the consistency between the results of CMT and corresponding prototype situations [11].

The 400 g-ton centrifuge at UCB was utilized to investigate the seismic performance of an earthen dam. Its maximum yielding mass and volume are 2 000 kg (19.6 kN) and 1.2×1.2×0.9 m^3, respectively. The distance from the swing platform to the rotated center of this centrifuge test device is about 5.49 m. It is capable of accelerating a 1 814.4 kg payload to a maximum of 200 g in 14 minutes and simulating earthquake motions in flight [26]. Base motion is actuated by a servo-hydraulic shaking table mounted on the swing platform. A maximum force of 42 kN can be delivered by the actuator of the shaking table.

From literatures and laboratory reports, Ni [27] reviewed the representative cross-sections, full water levels at the upper stream, soil distributions, and soil properties of the JenYiTan dam. Based on the representative configuration of this dam, three simplified 2D cross-sections were selected for the CMTs as shown in Figs.3(a), 4(a) and 5(a). All dimensions described below are in the prototype scale.

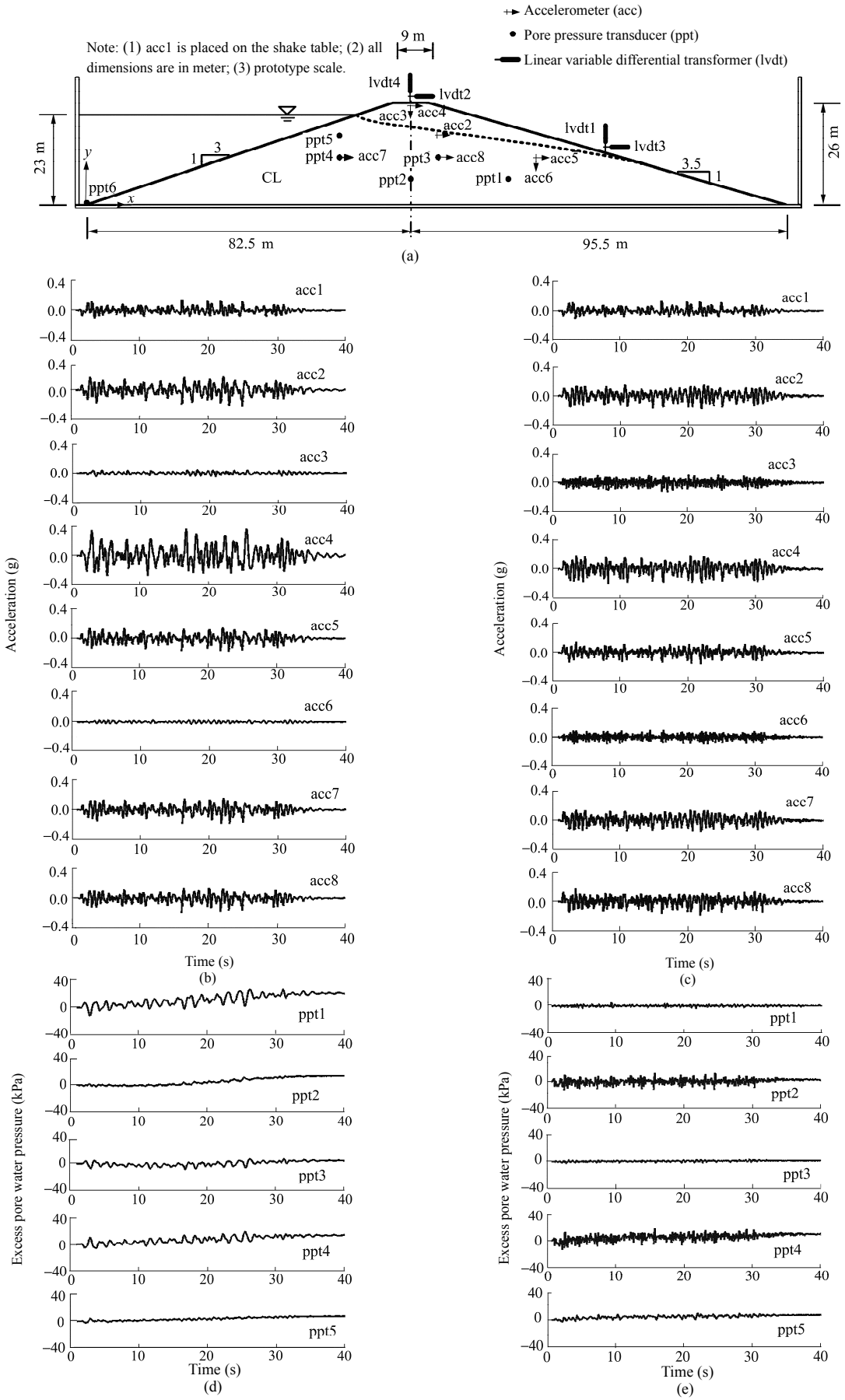

Fig.3 For the 1st model dam, (a) configurations, instrumental locations and the "simulated" (not measured) free surfaces of seepage using PLAXIS. The accelerations: (b) for the numerical models and (c) for the CMTs, and the excess pore water pressures: (d) for the numerical models and (e) for the CMTs.

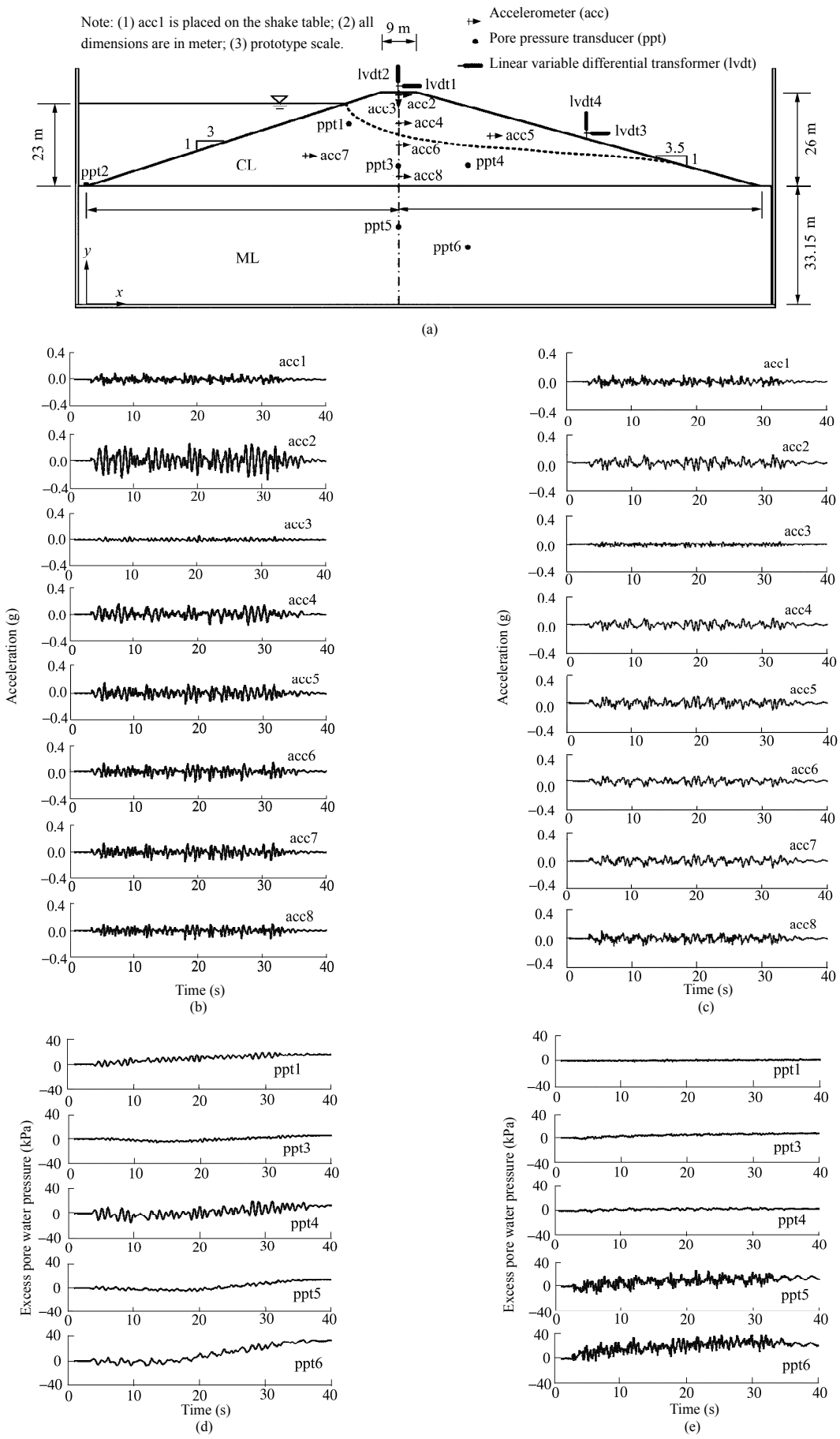

Fig.4 For the 2nd model dam, (a) configurations, instrumental locations and the "simulated" (not measured) free surfaces of seepage using PLAXIS. The accelerations: (b) for the numerical models and (c) for the CMTs, and the excess pore water pressures: (d) for the numerical models and (e) for the CMTs.

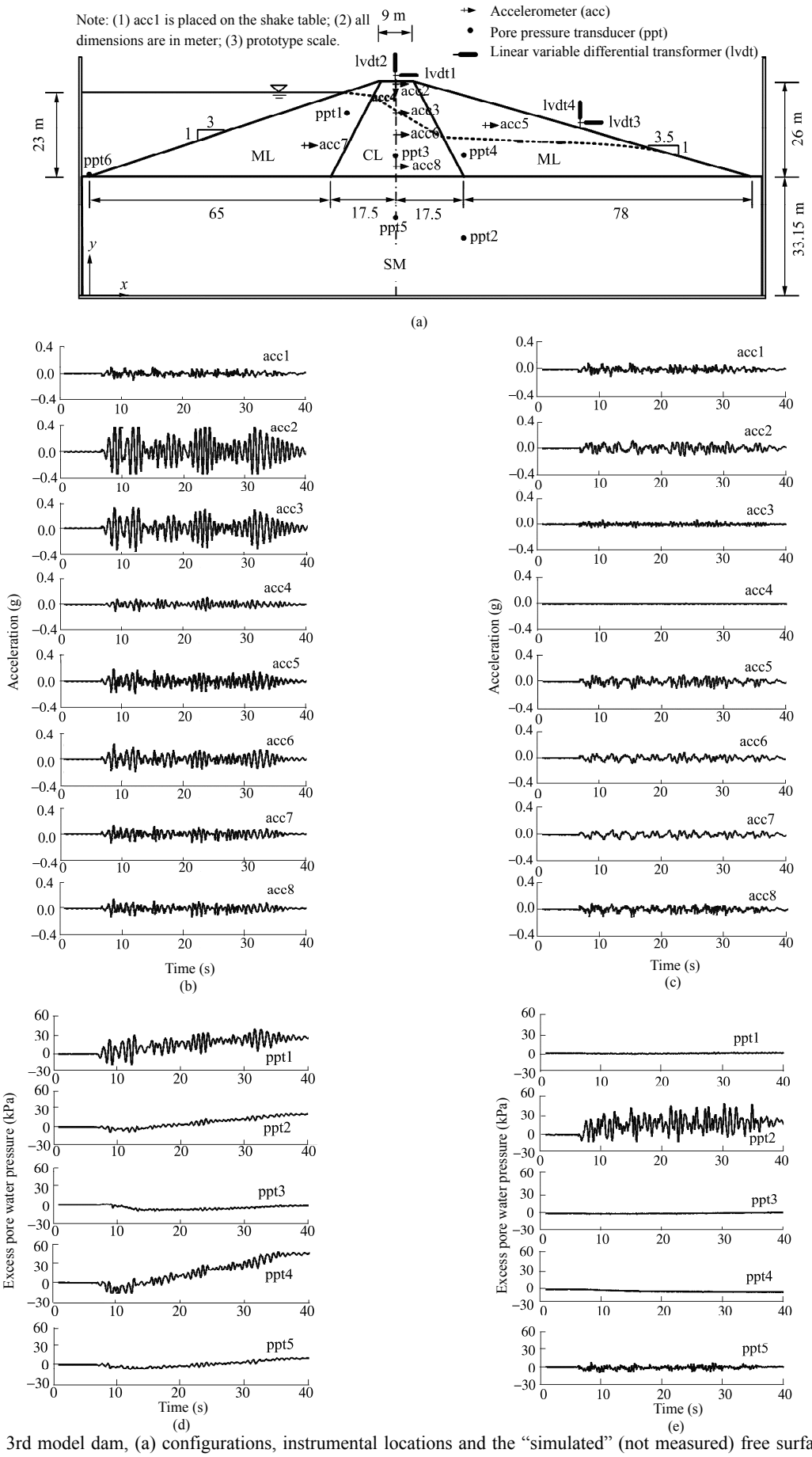

Fig.5 For the 3rd model dam, (a) configurations, instrumental locations and the "simulated" (not measured) free surfaces of seepage using PLAXIS. The accelerations: (b) for the numerical models and (c) for the CMTs, and the excess pore pressures: (d) for the numerical models and (e) for the CMTs.

The height of dam is 33.15 m and the width of crest is 9 m. The slopes are 1:3 (18.4°) and 1:3.5 (15.9°) for the upstream and downstream of these model dams, respectively, and 1:0.5 (63.4°) for the core of the 3rd dam. The depth of the foundations for the 2nd and 3rd model dams is 26 m. The initial upstream water level is 23 m from the toe of dam. The 1st and 2nd model dams, which are both made of low-plasticity clay (denoted by CL), are placed on a rigid base and foundation composed of low-plasticity silt (denoted by ML). The 3rd model dam was made of CL for the core, ML for the shell, and muddy sand (denoted by SM) for the foundation. These three kinds of soils, i.e. CL, ML, and SM, were sampled in the vicinity of the JenYiTan dam and their properties were tested conventionally in the laboratory at 1 g (Table 1).

Model responses were measured using miniature transducers. In each model dam, there were eight accelerometers (denoted by acc 1–8), six pressure transducers (represented by ppt 1–6), and four standard linear voltage displacement transformers (shown by LVDT 1–4). The locations of these transducers in prototype scale are listed in Table 2. The origin of the coordinates is set at the bottom-left corners of Figs.3(a), 4(a), and 5(a). The acceleration history recorded by acc1, which was horizontally mounted on the shaking table, was selected as the horizontal component of the base shaking for subsequent numerical models.

Considering the limited volume in the centrifugal test device, the scaling factor was taken to be N=150 in this study. Thus, all model dams were tested at a 150 g centrifugal acceleration field. Rigid boxes were selected as the model containers. The inside dimensions of two rigid-wall containers, made of 6 063 grade aluminum with a thickness of 1.27 cm, are 122 cm×30.5 cm×22.9 cm for the 1st model dam, and 122 cm× 30.5 cm×43.2 cm for the 2nd and 3rd model dams [28].

Water was used as the pore fluid instead of a more viscous fluid that may have had unwanted effects on the permeability, strength, stiffness, and damping characteristics of the soil [29]. From N =150, the width of container, i.e. 30.5 cm, the configurations of three cross-sections (shown in Figs.3(a), 4(a), and 5(a)), and the total unit weights of three kinds of soils (calculated by the dry unit weight and water content listed in Table 1), the total weights including the water in the reservoir are about 0.81, 2.56, and 2.46 kN for the 1st, 2nd, and 3rd CMT models, respectively.

The three model dams were all subjected to the same input motions, which were generated by SIMQKE [30] to be compatible with a specified target spectrum. To establish the target spectrum, we utilized the historical earthquake accelerograms of the M_L=6.4 ChiaYi earthquake of 22 October 1999. The peak acceleration (PA = 992 gal) was recorded at a station near the JenYiTan dam at ChiaYi in central Taiwan.

According to the scaling laws, the duration for a model in CMT was shortened to be 1/N times of that for the prototype earthquake. In addition, the amplitudes and frequencies of accelerations were N times larger for a model in CMT than those for the corresponding prototype. Due to the limited capacity of the shaking table, the corresponding prototype earthquake could not contain frequencies higher than (400/N) Hz, i.e. 2.67 Hz, for this study. To reduce the numerical error, frequencies higher than 2.5 Hz were filtered out from the prototype earthquake. Then, the filtered accelerations are numerically integrated twice to obtain the displacements for the displacement-controlled system of the shaking table.

Wooden molds and containers were used to construct the slopes and boundaries. There were nine layers (with a height of 1.91 cm per layer) for a model dam and six layers (with a height of 3.68 cm per

Table 1 Material properties of three types of soils.

Materials	Specific gravity G_s	Dry unit weight γ_{dry} (kN/m^3)	Saturated water content w (%)	Cohesion c (kPa)	Friction angle ϕ (°)	Poisson's ratio ν	Permeability k (10^{-5} m/s)
CL	2.71	18.2	18	40	25	0.3	1.29×10^{-5}
ML	2.67	19.0	15	60	31	0.3	2.63×10^{-3}
SM	2.66	17.5	17	30	38	0.3	4.09

Materials	Coefficient of consolidation	Coefficient of rebound	Ultimate stress ratio M_f	Turning-point stress ratio M_m	Parameter B (for saturated soils)	Parameter B_{dry} (for dry soils)
CL	0.033	0.013	1.36	0.45	2 000	250
ML	0.008	0.002	2.50	0.41	4 000	250
SM	0.010	0.003	2.50	0.41	5 000	—

Table 2 Coordinate locations of the transducers. m

Device	The 1st dam		The 2nd dam		The 3rd dam	
	x	*y*	*x*	*y*	*x*	*y*
acc2	89.00	17.15	82.50	59.15	82.50	59.15
acc3	82.50	26.00	82.50	59.15	82.50	54.64
acc4	82.50	26.00	82.50	54.64	82.50	59.15
acc5	114.01	11.43	107.51	46.98	107.51	46.98
acc6	114.01	11.43	82.50	44.58	82.50	44.58
acc7	64.00	11.43	57.50	41.72	57.50	41.72
acc8	89.00	11.43	82.50	36.00	82.50	36.00
ppt1	107.51	5.72	65.00	50.29	65.00	50.29
ppt2	82.50	5.72	0.00	33.15	100.01	16.57
ppt3	89.00	11.43	82.50	38.86	82.50	38.86
ppt4	64.00	11.43	100.01	38.86	100.01	38.86
ppt5	64.00	17.15	82.50	22.10	82.50	22.10
ppt6	0.00	0.00	100.01	16.57	0.00	33.15
lvdt1	132.45	13.00	82.50	59.15	82.50	59.15
lvdt 2	82.50	26.00	82.50	59.15	82.50	59.15
lvdt 3	132.45	13.00	132.45	46.15	132.45	46.15
lvdt 4	82.50	26.00	132.45	46.15	132.45	46.15

layer) for the foundations of the 2nd and 3rd model dams. A model was constructed layer by layer from bottom to top. A given amount of soil with a particular dry density and water content (listed in Table 1) was put into the container and then compacted until the correct layer thickness was reached. Trenches and holes were also made for installing wires and instruments at appropriate locations, if necessary.

When the construction was completed, the container with the model dam was mounted on the shaking table. Water then was slowly poured into the upstream side of this dam until the designed water level was obtained. Then, the transducers were connected to the data acquisition system. Afterwards, the centrifuge was spun into action from start-up to 150 g-level, and then the centrifugal acceleration was kept at 150 g to enable the seepage within the model dam to reach a steady state. When the base shaking was excited, all instruments in the model dam were simultaneously triggered by the vibrations.

Three model dams were tested following a similar procedure. The results of these three CMTs are compared with those from the numerical models in the next section.

4 Numerical simulations

The model dams were discretized using four-nodal quadrilateral elements, each with four Gauss points. The 1st model dam consisted of 555 elements and 493 nodes, whereas the 2nd and 3rd model dams and their foundations had 963 elements and 889 nodes.

Regarding the boundary conditions between each model dam and its container, the base of each model dam was fixed. For the 2nd and 3rd model dams, the lateral sides of the foundations were also fixed horizontally. In addition, the base and lateral boundaries of foundations were made impermeable.

Before performing numerical simulations, the initial stress and seepage for each model dam were analyzed using PLAXIS [31]. This code is a numerical program used for static and seepage analysis. The simulated (not measured) free surfaces of seepage (i.e. phreatic lines) are shown as dashed lines in Figs.3(a), 4(a) and 5(a). The elements above the phreatic lines were considered to be dry, with no degrees of freedom (DOF) of excess pore pressure.

Material parameters of the Oka constitutive law are summarized in Table 1. These parameters were experimentally determined at TUT by (1) physical property tests, permeability tests, consolidation tests, and drained compression tests under monotonic loading, and (2) undrained triaxial tests under cyclic loading. In view of the scaling laws applicable to centrifuge experiments, the prototype permeability at N g is N times its value at 1 g. Therefore, the permeability was multiplied by N for the numerical models.

Numerical modeling and CMT results are shown in Figs.3–5. The middle and lower diagrams show the acceleration and excess pore pressure histories, respectively. The histories of displacements measured at lvdt 1–4 are not available because the lvdts were found to have dismounted during the test [28].

To evaluate the reliability of the numerical models using code LIQCA, a normalized root-mean-square error (NRMSE) was used to assess the closeness of the fit between the simulated and recorded time histories. This was done by averaging the differences in corresponding values for the two time histories over the analysis time interval $t_1 \le t \le t_2$. To get a dimensionless index, this comparison index is divided by the maximum absolute recorded value.

Given two excess pore pressure time histories, i.e. p_{cmt} recorded from CMTs and p_{ns} simulated from numerical models, the NRMSE of p_{ns} with respect to p_{cmt} was computed from the following expression:

$$\varepsilon_{\mathrm{nrms}}(p) = \frac{\sqrt{\int_{t_1}^{t_2} [p_{\mathrm{ns}}(t) - p_{\mathrm{cmt}}(t)]^2 \,\mathrm{d}t}}{\max(|p_{\mathrm{cmt}}|)\sqrt{t_2 - t_1}} \tag{12}$$

where the denominator is a normalizing factor equal to the product of the maximum absolute value of p_{cmt} and the square root of duration $(t_2 - t_1)$. The duration is set to be 45 s.

Equation (12) indicates that the value of NRMSE decreases with increasing reliability of numerical models. However, a comparison based on the NRMSE index alone does not account for the reliability of the experimental results. If a large number of experiments are conducted under the same conditions, the reliability of the experimental results can be assessed by using other comparison indices, such as the standard deviation of numerous experimental results that are measured at a homologous location in each model dam. In this study, one experiment was made for each model dam. Therefore, the reliability of numerical models assessed by the NRMSE is based on the assumption that the experimental recordings are reliable.

The components of acceleration are more apparent in the frequency domain than in the time domain. Hence, the comparison index of acceleration was obtained by comparing the predicted Fourier spectra, FS_{ns}, with the recorded ones, FS_{cmt}, at frequency f ($f_1 \le f \le f_2$). Therefore, the NRMSE of FS_{ns} with respect to FS_{cmt} was computed as

$$\varepsilon_{\mathrm{nrms}}(FS) = \frac{\sqrt{\int_{f_1}^{f_2} [FS_{\mathrm{ns}}(f) - FS_{\mathrm{cmt}}(f)]^2 \,\mathrm{d}f}}{\max(FS_{\mathrm{cmt}})\sqrt{f_2 - f_1}} \tag{13}$$

where FS is the smoothed Fourier spectrum. The two specific frequencies are f_1=0 Hz and f_2=$f_{2,\mathrm{cmt}}$= $[(1/t_{\mathrm{p,cmt}})+3H_{\mathrm{cmt}}]$ Hz. Here, $t_{\mathrm{p,cmt}}$ is the predominant period, H_{cmt} is the bandwidth, and the subscript "cmt" denotes the value obtained from CMTs.

Both H and t_{p} can be determined from the smoothed Fourier spectrum. The maximum Fourier spectrum amplitude is at t_{p}. The bandwidth is the frequency range over a level of $1/\sqrt{2}$ times the maximum Fourier spectrum amplitude. In this bandwidth, the spectral amplitudes are dispersive about t_{p} [32]. The Fourier spectra are shown in Fig.6, with the Figs.6(a), (b), (c) diagrams for the numerical models and others for the CMTs. The original and smoothed Fourier spectra are displayed by the thin and thick lines, respectively. The maximum amplitude of the smoothed Fourier spectrum at t_{p} is marked by a circle. The position of $f_{2,\mathrm{cmt}}$ is denoted by a dashed line if $f_{2,\mathrm{cmt}}$ is less than 5 Hz.

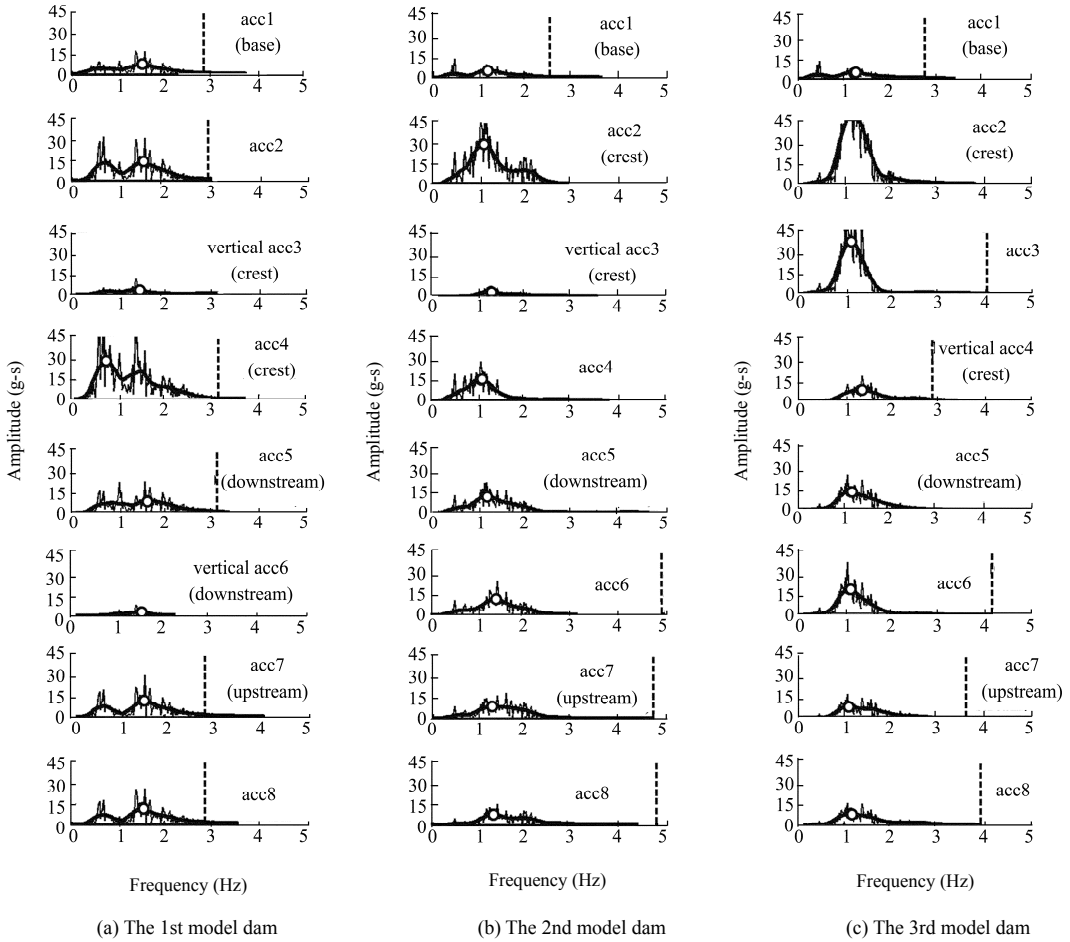

(a) The 1st model dam (b) The 2nd model dam (c) The 3rd model dam

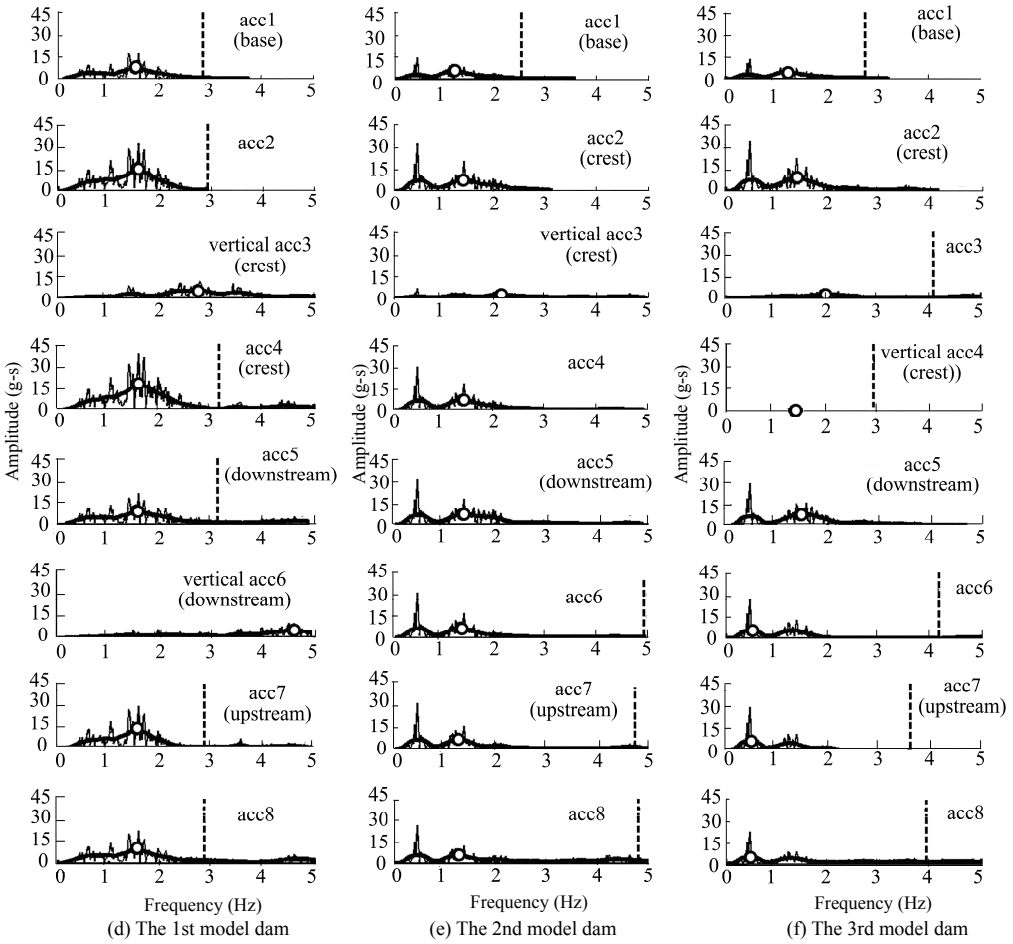

Fig.6 The Fourier spectra: (a)–(c) for the numerical models, (d)–(f) for the CMTs, (a) and (d) for the 1st model dam, (b) and (e) for the 2nd model dam, and (c) and (f) for the 3rd model dam.

Figure 6 shows that most of components are included in the range of (0–$f_{2,\mathrm{cmt}}$) Hz. The NRMSEs of acceleration and excess pore water pressure at measured positions in the three model dams are listed in Table 3.

Table 3 The normalized root-mean-square errors.

Device	The 1st model dam	The 2nd model dam	The 3rd model dam
acc2	0.133	0.941	1.489
acc3	0.364*	0.313*	4.555
acc4	0.405	0.457	12.415*
acc5	0.115	0.286	0.364
acc6	0.436*	0.318	0.833
acc7	0.119	0.329	0.481
acc8	0.119	0.330	0.466
ppt1	3.015	4.349	9.911
ppt2	0.537	—	0.263**
ppt3	0.938	0.602	2.355
ppt4	0.255	1.304	6.909
ppt5	0.215	0.295**	0.571**
ppt6	—	0.320**	—

Note: * These acc transducers are arranged for the vertical acceleration.
** These ppt transducers are placed at the foundation.

To conveniently compare the results, several indices of $\ddot{\boldsymbol{u}}$ and p, including the peak absolute acceleration PA, predominant period t_{p}, bandwidth H, and final excess pore water pressure F_{p}, were used. Table 4 shows the ranges of these indices: the upper rows for the CMTs and the lower rows with gray background for the numerical models.

The characteristics of base motions recorded at acc1 for the three model dams are 0.13, 0.1, and 0.1 g for PA; 0.66, 0.85 and 0.83 s for t_{p}; and 0.44, 0.44 and 0.51 Hz for bandwidth. The variances of these indices in terms of depth are shown in Fig.7, with Figs.7(a)–(d) for the numerical models, and Figs.7(e)–(h) for the CMTs. The indices for the 1st, 2nd, and 3rd model dams are displayed by a circle, cross, and triangle, respectively. The bottoms of the dam and foundation are –26 and –59.15 m below the crest, respectively. The initial stress gap can be written as $p_{\mathrm{z}} = I_0 - \sqrt{2}J_0 / M_{\mathrm{f}}$ where the subscript "0" denotes the initial value of invariance. The variance of F_{p} in terms of p_{z} for the numerical models is shown in Fig.8.

Table 4 The ranges of indices for acceleration and excess pore water pressure.

Model dam	Peak acceleration PA (g)	Predominant period t_p (s)	Band width H (Hz)	Excess pore water pressure F_p (kPa)	
				Within the dam	Within the foundation
1st	0.16 – 0.36	0.62 – 1.36	0.42 – 1.22	−12.4 – 26.6	—
	0.17 – 0.19	0.64 – 0.65	0.44 – 0.53	−11.6 – 19.0	—
2nd	0.13 – 0.27	0.74 – 0.98	0.44 – 0.91	−15.3 – 20.2	−7.5 – 33.7
	0.07 – 0.13	0.74 – 0.79	1.15 – 1.58	−2.0 – 8.0	−11.9 – 38.8
3rd	0.13 – 0.45	0.83 – 0.91	0.40 – 0.67	−21.9 – 49.6	−8.5 – 21.0
	0.07 – 0.13	0.52 – 2.14	0.71 – 1.53	−4.3 – 2.3	−18.9 – 52.7

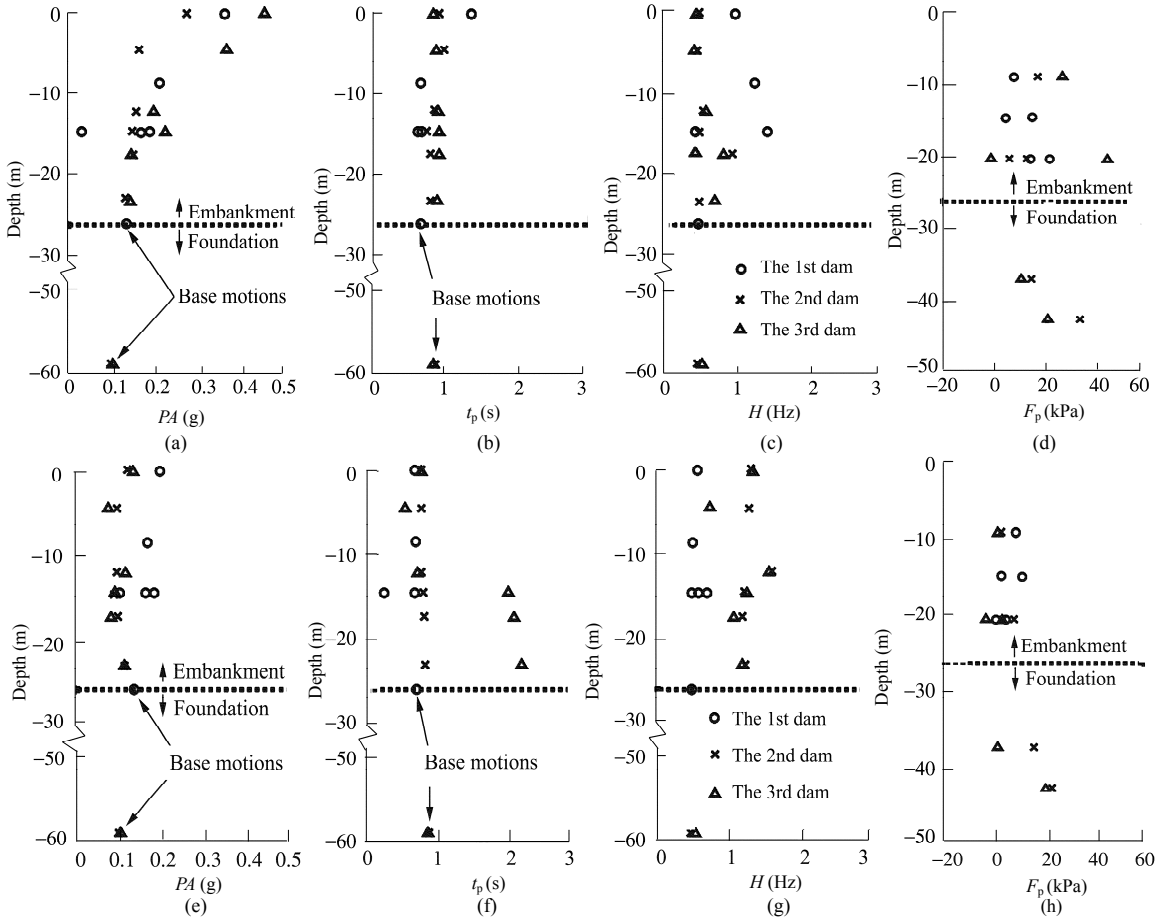

Fig.7 The variances of indices in terms of depth.

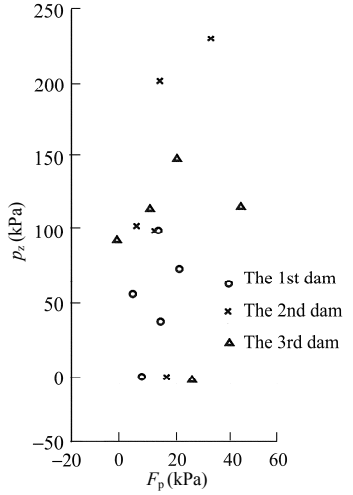

Fig.8 The variances of final excess pore pressure in terms of initial stress gap for the numerical models.

Regarding the recorded acceleration history at acc3 in the 3rd model dam, the frequency components (Fig.6(f)) and the amplitudes of accelerations (Fig.5(d)) are very small when compared with other recorded horizontal accelerations. This indicates that accelerometer acc3 might have been malfunctioned. Therefore, this record is not discussed further.

Five records of excess pore water pressures (Figs.3(e), 4(e) and 5(e)) show that the amplitudes of oscillation and the values of F_p are both small at related recording sites, including ppt1 and ppt4 for the 2nd model dam, and ppt1, ppt3 and ppt4 for the 3rd model dam. This indicates a likely malfunction in the pressure transducers at these locations and, therefore, these records of excess pore water pressures are not discussed further.

In contrast, there are six distinct oscillations of excess pore pressure that were recorded at ppt2 and ppt4 for the 1st model dam, ppt5 and ppt6 for the 2nd model dam, and ppt2 and ppt5 for the 3rd model dam. These ppt transducers were located at a deeper layer than the malfunctioning ppt transducers.

5 Discussion

5.1 Reliability of the LIQCA model

Regardless of measured vertical accelerations (i.e. acc3 and acc6 for the 1st model dam, acc3 for the 2nd model dam, and acc4 for the 3rd model dam), the mean values of $\varepsilon_{\text{nrms}}(FS)$ for the three model dams increase from the 1st to 3rd model dams (Table 3). The values of $\varepsilon_{\text{nrms}}(FS)$ at acc5 in the downstream are smaller than those at acc7 in the upstream. In general, the values of $\varepsilon_{\text{nrms}}(FS)$ for the horizontal accelerations increase from bottom to crest. The values of $\varepsilon_{\text{nrms}}(FS)$ for the vertical accelerations at the crest are 0.364, 0.313, and 12.415 in the 1st, 2nd, and 3rd model dams, respectively.

The assessment described above leads to the following four main observations.

(1) Similarity between simulated and recorded acceleration histories decreases from the 1st to the 3rd model dam.

(2) Similarity is lower in the upstream than in the downstream for each model dam.

(3) Similarity is lowest at the crest than at other places in each model dam.

(4) Similarity for the vertical accelerations is not clear due to lack of the measured base vertical acceleration for the input shaking motions.

The mean values of $\varepsilon_{\text{nrms}}(p)$ for the three model dams also increase from the 1st to 3rd models (Table 3). For the 1st model dam, the values of $\varepsilon_{\text{nrms}}(p)$ at ppt4 and ppt5 at the upstream side of the model are smaller than those at ppt1, ppt2, and ppt3 on the downstream side. For the 2nd and 3rd model dams, the values of $\varepsilon_{\text{nrms}}(p)$ in the foundation are smaller than those in the dam. In addition, the values of $\varepsilon_{\text{nrms}}(p)$ near the interface between the CL core and ML shell for the 3rd model dam are the largest. These results lead to the following four main observations.

(1) Similarity between the simulated and recorded excess pore water pressure histories decreases from the 1st to 3rd model dams.

(2) Similarity is lower at the downstream side of the 1st model dam than at the upstream side.

(3) Similarity is lower in the dam than in the foundation for the 2nd and 3rd model dams.

(4) Similarity is lowest at the interface of the 3rd model dam.

A reason for observation (1) is that higher complexity of soil distribution results in lower similarity. From observations (2) and (3), we infer that similarity is lower at positions near the simulated phreatic line than that at positions far from the simulated phreatic line for each model dam. One possible reason for this is the difference between the simulated and experimental seepage conditions.

Although a "spinning time" was imposed in the CMTs to reach a steady state of seepage prior to shaking, this steady state was not confirmed. The gradual evaporation of water by high-speed wind during the centrifugal spin-up could have lowered the water level of a modeled reservoir and the phreatic line in the embankment, especially at the downstream side (e.g. ppt1 for the 1st model dam, ppt4 for the 2nd and 3rd model dam). Therefore, unsaturated soils around the ppt devices could reduce the reliability of measurements.

To reduce this kind of error, trial tests should be conducted before executing the CMTs to confirm consistency between the designed and tested seepage conditions. Further studies of the measurement methods and construction process are needed to understand the seepage in a model dam.

5.2 Variances of indices

The average t_{p} for the 1st, 2nd, and 3rd model dams are 0.65, 0.85 and 0.88 s for the numerical models, and 0.65, 0.75 and 0.60 s for the CMTs, respectively. The bandwidths are less than 1.6 Hz. This indicates that the major part of the spectral amplitudes is dispersed in the range of $(1/t_{\text{p}} - 0.5H)$ to $(1/t_{\text{p}} + 0.5H)$, i.e. 0.7–2.3 Hz. In addition, the results of the horizontal accelerations from CMTs show that the magnification of horizontal *PA* is higher for a dam located on a rigid base than that for a dam positioned on soil layers.

As mentioned above, the horizontal peak accelerations of CMTs occur over a small range for the 2nd and 3rd model dams, but increase from the rigid base to the crest for the 1st model dam. In contrast, the magnification of the horizontal peak acceleration is high for numerical models. The t_{p} and the first two f_{p} of horizontal accelerations of the numerical models agree with those of the CMTs, but the number of peaks, the bandwidth,

and the frequency distribution of the Fourier spectrum do not. The numerical results show that the soil elements near the crest are close to liquefaction or failure during an earthquake, but liquefaction was not observed on the crest of three model dams in the CMTs. Hence, a liquefied soil with little stiffness is more "shakable" than that with a higher stiffness.

This leads to the fact that the peak accelerations for the numerical models are larger than those for the CMTs, and the values of $\varepsilon_{\text{nrms}}(FS)$ of horizontal accelerations increase from bottom to crest. This also produces the inconsistency in the frequency distribution observed in the Fourier spectra of these two approaches. Therefore, the lower stiffness of soil at the crest that was used in the numerical models could be incorrect. In other words, the mechanism of stiffness degradation in the Oka constitutive law is not adequate.

The two biggest observed differences in F_{p} between the numerical models and CMTs are 49 kPa at ppt4 and 38 kPa at ppt1 (Figs.7(d) and (h)) for the 3rd model dam, which are located near the interface between the CL core and ML shell. This shows the difficulty in simulating the motions of the interface boundary between two types of soils.

Regardless of F_{p} at ppt1 and ppt4 for the 3rd model dam, a positive correlation between F_{p} and depth can be shown (Fig.7(d) and (h)). Higher F_{p} is excited at the foundation than in the dam. Figure 8 shows that F_{p} increases with p_{z} in the numerical models. This indicates that F_{p} is high at locations where initial stress is exerted without reaching plastic yield. The possible reason for this is described below.

Since the duration of an earthquake is short, a small decrease in the magnitude of pressure resulting from drainage can be ignored. Therefore, the results of the undrained triaxial shear test [33] (Fig.9) can be used to explain the relationship between F_{p} and p_{z}. When soils are subjected to a cyclic shear load, p gradually increases with the load, whereas σ_{m} decreases (Figs.9(a) and (c)). In the undrained condition, the magnitude of the increasing pressure is equal to that of the decreasing σ_{m}. Hence, a simple interpretation is that the difference of σ_{m} from the initial to yield stresses dominates the ultimate magnitude of the pressure. In other words, p_{z} dominates the variation in F_{p}. In the conventional triaxial tests, the lateral stresses are equal, i.e. $\sigma_2 = \sigma_3$. This leads to $I = \sigma_{\text{m}}$ and $J = q/\sqrt{3}$, where q is a deviatoric axial stress.

Since $M_{\text{f}} = (\sqrt{2}J/I)_{\text{critical}} = \sqrt{2/3}(q/\sigma_{\text{m}})_{\text{critical}}$, the

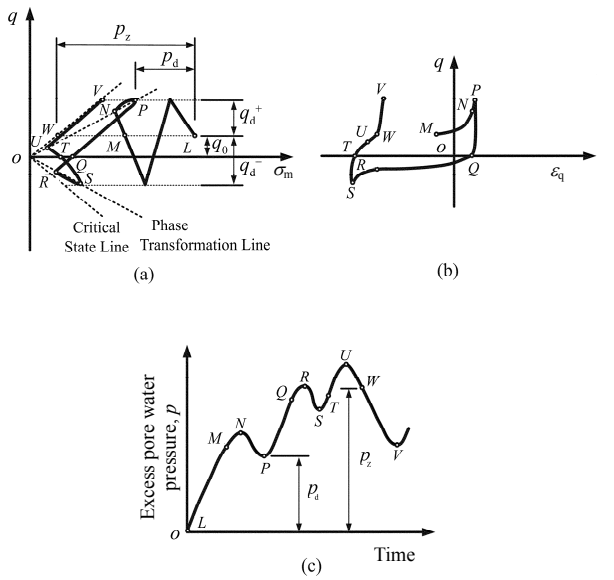

Fig.9 Results of triaxial undrained shear test: (a) for the stress path, (b) for the deviatoric strain-stress curve, and (c) for the excess pore water pressure history [33].

initial stress difference is given as

$$p_{\text{z}} = \sigma_{\text{m0}} - \sqrt{2/3}(q_0/M_{\text{f}}) = \sigma_{\text{m0}} - \frac{q_0}{(q/\sigma_{\text{m}})_{\text{critical}}} \tag{14}$$

Considering the amplitude of the cyclic shear stresses, the value of the pressure difference p_{d} is given as

$$p_{\text{d}} = \min\left(\sigma_{\text{m0}} - \sqrt{\frac{2}{3}}\left(\frac{q_0 + q_{\text{d}}^+}{M_{\text{m}}}\right), \sigma_{\text{m0}} - \sqrt{\frac{2}{3}}\left(\frac{-q_0 + q_{\text{d}}^-}{M_{\text{m}}}\right)\right) \tag{15}$$

at the first time that the stress intersects the line of M_{m}. The measuring methods of p_{z} and p_{d} are shown in Figs.9(a) and (c), respectively.

Due to similarities in measured locations, soil properties, and initial stresses, the variations of p at ppt2 for the 1st model dam and at ppt3 for the 2nd and 3rd model dams are also similar. They provide the evidence to support the existence of a positive correlation of p_{z} versus F_{p}, i.e. $p_{\text{z}} \propto F_{\text{p}}$. Nevertheless, other factors, including the amplitude of the acceleration, the duration of earthquake, and soil properties, can also influence F_{p}. Therefore, the values of F_{p} at different locations could be different, even if the initial stresses and soil properties are the same at all locations.

6 Conclusions

For three simplified cross-sections of the JenYiTan dam, histories of ground acceleration and excess pore water pressure have been obtained from numerical

simulations and centrifugal modeling tests. Three significant observations have been made.

(1) The magnification of horizontal peak acceleration is higher for a dam on a rigid base than for one located on soil layers.

(2) The amplitudes of horizontal acceleration dominantly lie in the range of 0.7–2.3 Hz.

(3) The ultimate level of excess pore water pressure is dominated by difference in the effective mean stress between the initial and yield conditions.

The phenomenon can be explained by using the results of the undrained triaxial shear test.

To account for the reliability of the numerical models using the LIQCA code, a normalized root-mean-square error is used as a comparison index to assess the closeness between the simulated and recorded histories. Assuming that the experimental records are reliable, the assessment leads to the following main conclusions.

(1) The similarity between the simulated and recorded data, i.e. the acceleration and excess pore water pressure histories, decreases from the 1st to 3rd model dams due to the increasing complexity of soil distribution.

(2) The similarity of the excess pore pressure is lowest in the interface between two types of soils.

(3) The similarity is lower at the positions near the simulated phreatic line than at positions far from the simulated phreatic line for each model dam. One possible explanation is that experimental evaporation leads to a difference between the simulated and experimental seepage conditions.

(4) In general, the similarity of horizontal acceleration decreases from bottom to crest due to a lower stiffness of soil at the crest in the numerical models.

(5) The similarity of vertical acceleration is not clear due to lack of measurements of the base vertical acceleration for the input shaking motions.

(6) The LIQCA code is validated by a comparison between the numerical and centrifugal test results. Further studies of the mechanisms of stiffness degradation of soil under cyclic load, the motions of the interface between two types of soils, and the measurement methods and construction process for seepage in a centrifugal model dam, are needed.

Acknowledgments

The first author would like to express his heartfelt thanks to Dr. J. H. Wang (IES) and one anonymous reviewer for the valuable comments and corrections to improve the article.

References

[1] Mononobe N, Takata A, Matumura M. Seismic stability of earth dams. In: Proceedings of the 2nd Congress of Large Dams. Washington, D.C.: [s.n.], 1936: 435–442.

[2] Seed H B, Martin G R. The seismic coefficient of earth dam design. Journal of the Soil Mechanics and Foundations Division, ASCE, 1966, 92 (3): 25–58.

[3] Makdisi F I, Seed H B. Simplified procedure for evaluating embankment response. Journal of the Geotechnical Engineering Division, ASCE, 1979, 105 (12): 1 427–1 434.

[4] Newmark N M. Effects of earthquakes on dams and embankments: fifth Rankine lecture. Geotechnique, 1965, 15 (2): 139–159.

[5] Kokusho T, Ishizawa T. Energy approach to earthquake-induced slope failures and its implications. Journal of Geotechnical and Geoenvironmental Engineering, 2007, 133 (7): 828–840.

[6] Bray J D, Travasarou T. Simplified procedure for estimating earthquake-induced deviatoric slope displacements. Journal of Geotechnical and Geoenvironmental Engineering, 2007, 133 (4): 381–392.

[7] Ozkan M Y. A review of considerations on seismic safety of embankments and earth and rock-fill dams. Soil Dynamics and Earthquake Engineering, 1998, 17 (7–8): 439–458.

[8] Aydingun O, Adalier K. Numerical analysis of seismically induced liquefaction in earth embankment foundations, part I. Benchmark model. Canadian Geotechnical Journal, 2003, 40 (4): 753–765.

[9] Yang Z, Elgamal A, Adalier K, et al. Earth dam on liquefiable foundation and remediation: numerical simulation of centrifuge experiments. Journal of Engineering Mechanics, 2004, 130 (10): 1 168–1 176.

[10] Popescu R, Prevost J H. Centrifuge validation of a numerical model for dynamic soil liquefaction. Soil Dynamics and Earthquake Engineering, 1993, 12 (2): 73–90.

[11] Popescu R, Prevost J H. Comparison between VELACS numerical "class A" predictions and centrifuge experimental soil test results. Soil Dynamics and Earthquake Engineering, 1995, 14 (2): 79–92.

[12] Popescu R, Prevost J H. Reliability assessment of centrifuge soil test results. Soil Dynamics and Earthquake Engineering, 1995, 14 (2): 93–101.

[13] Wu Chunhsien. Numerical analysis of seismic motion for an earth dam. PhD Thesis. Taipei: Taipei University of Technology, 2002 (in Chinese).

[14] Ni Chihkuan, Yang Tengfang, Wu Chunhsien. A study of seismic motion for an earth dam. In: The 10th Conference on Current Researches in Geotechnical Engineering in Taiwan. Taipei: [s.n.], 2003: 103–106 (in Chinese).

[15] Lin Chunfu. Dynamic analysis of an earth dam using SWANDYNE. PhD Thesis. Taipei: Taipei University of Technology, 2004 (in Chinese).

[16] Wu Shaowei. Dynamic analysis for an earth dam using FLAC. PhD Thesis. Taipei: Taipei University of Technology, 2004 (in Chinese).

[17] Biot M A. Mechanics of deformation and acoustic propagation in porous media. Journal of Applied Physics, 1962, 33 (4): 1 482–1 498.

[18] Newmark N M. A method of computation for structural dynamics. Proc. ASCE, 1959, 85 (EM3): 67–94.

[19] Oka F, Yashima A, Shibata T, et al. FEM-FDM coupled liquefaction analysis of a porous soil using an elastoplastic model. Applied Scientific Research, 1994, 52 (3): 209–245.

[20] Oka F. A cyclic elasto-viscoplastic constitutive model for clay based on the non-linear hardening rule. In: Proceedings of the 4th International Symposium on Numerical Models in Geomechanics. Swansea: [s.n.], 1992: 105–114.

[21] Oka F, Yashima A, Tateishi A, et al. A cyclic elasto-plastic constitutive model for sand considering a plastic-strain dependence of the shear modulus. Geotechnique, 1999, 49 (5): 661–680.

[22] Oka F, Uzuoka R, Tateishi A, et al. A cyclic elasto-plastic model for sand and its application to liquefaction analysis. In: Constitutive Modelings of Geomaterials, Selected Contributions from the Frank L. DiMaggio Symposium. [S.l.]: [s.n.], 2002: 75–99.

[23] Uzuoka R, Sento N, Kazama M, et al. Three-dimensional numerical simulation of earthquake damage to group-piles in a liquefied ground. Soil Dynamics and Earthquake Engineering, 2007, 27 (5): 395–413.

[24] Uzuoka R, Cubrinovski M, Sugita H, et al. Prediction of pile response to lateral spreading by 3D soil-water coupled dynamic analysis: shaking in the direction perpendicular to ground flow. Soil Dynamics and Earthquake Engineering, 2008, 28 (6): 436–452.

[25] Tan T S, Scott R F. Centrifuge scaling considerations for fluid particle systems. Geotechnique, 1985, 35 (4): 461–470.

[26] University of Colorado at boulder website [OL]. [2008-01-01]. http://civil.colorado.edu/web/grad/geotech/faci/centrifuge/bigcentrifuge. html.

[27] Ni Chihkuan. Seismic evaluation of JenYiTan dam. Taipei: Taipei University of Technology, 2005 (in Chinese).

[28] Ge Yuning, Bao Yu, Ko H Y. Dynamic centrifuge model testing of Jenyitan dam. Boulder: University of Colorado, 2004.

[29] Zeng Z. Several important issues related to liquefaction study using centrifuge. In: Proc. Int. Symp. Physics and Mechanics of Soil Liquefaction. [S.l.]: [s.n.], 1999: 283–293.

[30] Gasparini D A, Simqke V E. User's manual and documentation. Massachusetts: Department of Civil Engineering, Massachusetts Institute of Technology, 1976.

[31] Brinkgreve R B J, Vermer P A. PLAXIS, finite element code for soil and rock analyses (ver 7.0). Rotterdam: Broodfield, 1998.

[32] Kramer S L. Geotechnical earthquake engineering. [S.l.]: Prentice Hall Inc., 1996.

[33] Muraleetharan K K, Deshpande S, Adalier K. Dynamic deformations in sand earth and rockfill dam: centrifuge modeling and blind, fully coupled analyses. Canadian Geotechnical Journal, 2004, 41 (1): 66–68.